The effects of vacancy ordering on diffusion: a statistical study

J Carter Stotts[1,*] ⓘ**, Xiaochuan Tang**[2]**, Gregory B Thompson**[3,4] **and Christopher R Weinberger**[1,2]

[1] School of Materials Science and Engineering, Colorado State University, Fort Collins, CO, United States of America
[2] Department of Mechanical Engineering, Colorado State University, Fort Collins, CO, United States of America
[3] Department of Metallurgical & Materials Engineering, The University of Alabama, Tuscaloosa, AL, United States of America
[4] Alabama Materials Institute, University of Alabama, Tuscaloosa, AL, United States of America

E-mail: carter.stotts@colostate.edu

CrossMark

Abstract

In this paper we investigate the interconnection between vacancy-ordered phases and vacancy self-diffusion. Here, we investigate three ordered phases on a square lattice with energetics defined by two separate Hamiltonians. In the first case we used a classical antiferromagnetic Ising model Hamiltonian in order to generate a 'checkerboard' type ordered structure. In the second case, we used a modified Ising model with competing influence of second and third nearest-neighbors, which resulted in both 'hatch' and 'labyrinthine' structures, depending on concentration. To understand how vacancy-ordering affects diffusion, we determined the tracer diffusivity using rejection-free kinetic Monte Carlo and compared disordered and ordered structures. Finally, we developed an analytical model describing diffusion in the ordered 'checkerboard' structure and found that it was able to predict apparent activation energies in the ordered and disordered structures. Our results suggest that it is short-range order rather than long-range order that most significantly affects tracer diffusion.

Keywords: short range order, long range order, correlation effects, diffusion, Ising model, kMC, Monte Carlo

1. Introduction

Some crystallographic systems contain a lattice or sublattice composed of a binary mixture of atoms and structural vacancies. At high temperatures, the arrangement of atoms and vacancies in these structures is completely random; however, at low temperatures ordered superlattices of structural vacancies are formed, similar to the ordered superlattices formed by ordered substitutional alloys. Studies on the effects of ordering on diffusion in ordered substitutional alloys have shown that ordered phases generally exhibit greater activation energies for diffusion compared to unordered phases, e.g. α_2-TiAl versus α-Ti [1–6]. Similarly, vacancy ordering is likely to affect diffusion in vacancy-ordered lattices.

Despite the obvious similarity between diffusion in ordered substitutional alloys and vacancy-ordered structures, there are two important differences. First, vacancies, the carriers of diffusion, are themselves ordering in addition to atoms. Second, the diffusion occurs by a mechanism involving structural vacancies rather than thermal vacancies and thus vacancy formation energy does not contribute to the thermally activated

---

* Author to whom any correspondence should be addressed.

behavior of the diffusion. The fact that the structural vacancies themselves are forming ordered structures may have important implications on the diffusion since there is an energetic predilection for vacancies to remain in low energy ordered configurations. This preference for order is likely to inhibit diffusion. On the other hand, some ordered structures possess networks of vacancies with low energy barriers that may act as high diffusivity pathways in a manner similar to dislocation pipe diffusion for vacancies [7, 8]. Under these circumstances, it is conceivable that vacancy-ordered structures could demonstrate an increase in diffusivity.

Perhaps the most important materials demonstrating vacancy ordering effects on diffusion are the intercalated lithium metal oxides. The lithium metal oxides have become ubiquitous in portable energy storage systems and as a result lithium diffusion in the metal oxides has been the topic of many studies [9–15]. Despite this, the effects of vacancy ordering on diffusion have not been studied. This is likely because the effects of vacancy ordering are often difficult to separate from other concentration-dependent mechanisms such as divacancy diffusion, tri-vacancy diffusion, and metal ion valency [16–18]. Nevertheless, there is evidence that the lithium diffusivity in $LiCoO_2$ has a minimum with respect to lithium concentration at the concentrations coinciding with the vacancy ordered phase boundaries, i.e. the minimum and maximum Li concentrations of the vacancy-ordered Li_xCoO_2 phase [19, 20].

In another group of materials, the transition metal carbides and nitrides, the effects of vacancy ordering on hardness and magnetic susceptibility have been documented, with the former increasing as a function of ordering and the latter decreasing [21–24]. The effect of vacancy ordering on vacancy self-diffusion; however, has not been the subject of any studies. The best evidence for order effects on diffusion in these materials comes from a study on the effects of carbon concentration on carbon diffusion in substoichiometric titanium carbide. In his study, Sarian found that the apparent activation energy for carbon diffusion nearly doubled at a temperature of 2080 °C in $TiC_{0.67}$ [25]. Sarian attributed this observed change in apparent activation energy to a vacancy order-disorder transition occurring on the carbon sublattice of the B1 rocksalt (NaCl-type) structure; though more recent thermodynamic studies conducted by Gusev *et al* have indicated that the long range order (LRO)-disorder transition occurs at a much lower temperature [26–29]. If Sarian's anomaly is indeed a consequence of ordering, it raises the question of how ordering actually affects diffusion and if it is related to short-range ordering (SRO) or LRO.

There is speculation that SRO may influence many material behaviors. Multicomponent solid solutions, especially high entropy materials such as high entropy alloys and high entropy ceramics [30–34] have grown in popularity over the past two decades [35]. These materials systems involve equimolar mixtures containing five or more alloying elements with the intention of improving phase stability by driving up the configurational entropy of the mixture [36–38]. High entropy materials are often reported to have exceptional mechanical, thermodynamic, and functional properties [39–41]. Several

mechanisms are proposed to contribute to the improved properties, including SRO effects due to preferential pair-bonding of alloying elements [42]. It is especially likely that SRO can dramatically affect kinetic processes in these high entropy materials, whose improved properties are often attributed in part to 'slow diffusion' [43–45].

In studies on two-dimensional lattice-gas adsorption systems 'memory effects' have been shown to have profound effects on tracer and collective diffusivities within two-dimension ordered phases as well as near phase transition boundaries [46, 47]. In particular, the hop correlation factor has been shown to be heavily dependent on composition/coverage in these systems as well as having a profound effect on the apparent activation energy. Previous authors have described these effects by writing the tracer diffusivity as a rate equation containing separate terms for each type of hop and accounting for hop multiplicity [48, 49]. Using this formulation, the apparent activation energy can be understood as a weighted average of hops having different energy barriers. Importantly, this framework highlights how the apparent activation energy can change as a function of temperature and composition due to the corresponding changes in hop multiplicity [48, 50].

From this brief review of the literature, it is evident that diffusion on vacancy-ordered sublattices represents an interesting and understudied intersection between two fundamental physical phenomena: vacancy order-disorder transformations and tracer diffusion. The effects of vacancy ordering on the tracer diffusivity and its apparent activation energy are generally not known. Furthermore, it is unclear if LRO or SRO is responsible for observed changes in hop correlation factor. In this work, we conduct Monte Carlo (MC) and kinetic MC (kMC) simulations on a square lattice consisting of A atoms and structural vacancies in order to garner insight into the effects of vacancy ordering on tracer diffusion.

2. Methodology

2.1. MC simulation

To capture ordering effects, we used two different model Hamiltonians with repulsive interactions. The first was a classical antiferromagnetic nearest neighbor Ising model [51–53] as shown in equation (1) resulting in a 'checkerboard' type ordered structure. The second Hamiltonian, shown in equation (2), was constructed in order to create an energetic preference for second nearest neighbors to be of like type and third nearest neighbors to be of unlike type, i.e. a Hamiltonian with competing second-nearest and third-nearest neighbor mechanisms [54, 55], resulting in a 'labyrinthine' structure consisting of rows or columns having the same type of sites. These rows or columns of vacancies hypothetically act as high-diffusivity pathways which may influence diffusion. Here, $J_1 = -1c$ is the interaction coefficient which we have chosen in the first case and $J_2 = -0.25c$ in the second, where we have defined the constant $c = k_B * 1K$ in order to give our interaction coefficients the correct units. The second interaction coefficient was chosen to be smaller in order to

a)

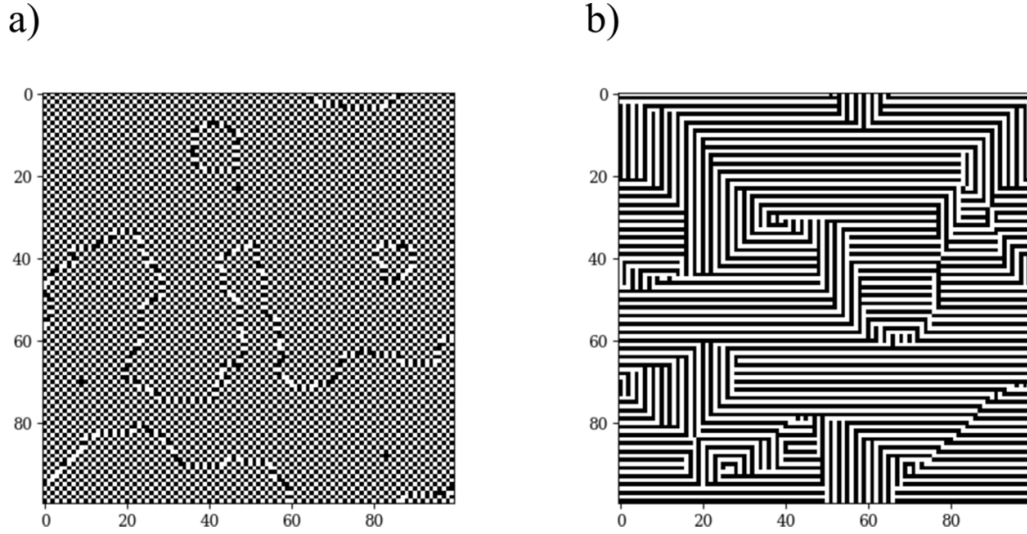b)

Figure 1. (a) The 'checkboard' structure produced by the Hamiltonian shown in equation (1). (b) The 'labyrinthine' structure produced by the Hamiltonian shown in equation (2).

make the energies more comparable between the structures. The spin variables σ take on values of 1 or -1 depending on if the site is occupied by an atom or a vacancy. σ_i is the spin variable of the ith site and σ_j, σ_k and σ_l are the spin variables of sites in the first, second, and third neighbor shells respectively. Thus, the 'checkboard' structure is constructed by creating a repulsive force between nearest neighbors of the same spin and the 'labyrinthine' structure is constructed by creating an attractive force between second nearest neighbors of same spin and a repulsive force between third nearest neighbors of the same spin,

$$\mathcal{H} = -\frac{1}{2}J_1 \sum_{ij} \sigma_i \sigma_j \tag{1}$$

$$\mathcal{H} = \frac{1}{2}J_2 \left(\sum_{ik} \sigma_i \sigma_k - \sum_{il} \sigma_i \sigma_l \right) . \tag{2}$$

The canonical ensemble was then sampled to generate structures and determine equilibrium properties using Kawasaki Dynamics [56], i.e. for each transition the system's total spin (vacancy concentration) was conserved by proposing to swap the spins of any two sites. In essence, for any swap to be meaningful it must occur between sites with unlike spin, since swapping sites with the same spin has no effect on the energetics or configuration of the system. This process was carried out for 1000 MC steps on a 30×30 square lattice, where each MC step consisted of a single sweep of the lattice wherein the spin variables at two sites were proposed to be swapped, i.e. a single MC step was considered to have completed after the number of proposed swaps was equal to the number of sites on the lattice. The change in energy was calculated for each proposed swap and swaps resulting in a reduction in energy were automatically accepted whereas swaps resulting in an increase in energy were accepted according to Boltzmann's distribution, equation (3), where $\Delta\mathcal{H}$ is the change in energy, k_B is the Boltzmann constant,

and T is the simulation temperature. For swaps resulting in an energy increase, a random number $u_1 (0, 1)$ was generated and the swap was accepted if $u_1 < P(\Delta\mathcal{H}, T)$, i.e. with the probability determined by equation (3),

$$P(\Delta\mathcal{H}, T) = \exp\left(-\frac{\Delta\mathcal{H}}{k_B T} \right) . \tag{3}$$

Sample equilibrium structures are shown in figure 1 for the (a) checkerboard structure and (b) labyrinthine structure at very low temperatures, illustrating the nature of low temperature order. Shown in figure 2 is the energy per site versus MC step for the 'checkerboard' (blue triangles) and 'labyrinthine' (red squares) simulations at $k_B T = 1.0$. After 300 MC steps, represented by the dashed vertical line, the system was considered to be in equilibrium.

2.2. kMC simulation

The rejection free kinetic MC method was employed in order to model atomic migration. The energy barrier ΔH^* for each event was then calculated via equation (4) where ΔH is a direction-independent kinetically resolved activation energy, in other words, an energy barrier formulated using the Brønsted–Evans–Polanyi principle [17, 57]. Here, we have made the assumption that all of the diffusion transition states occur at the same energy level, chosen as $15c$ arbitrarily in order to prevent negative, and therefore physically meaningless, activation energies. $\Delta\mathcal{H}$ is the difference in energy between the final and initial configurations of the selected event. During the simulation, before an event was selected to be carried out, a rate catalogue was constructed by determining the energy barrier associated with all of the possible jumps that could be made by each vacancy. The possible jumps were restricted to nearest-neighbor sites with opposite spin. For each vacancy-atom pair the system energy was determined from equation (1) for the 'checkerboard' structure and equation (2) for the 'labyrinthine' structure,
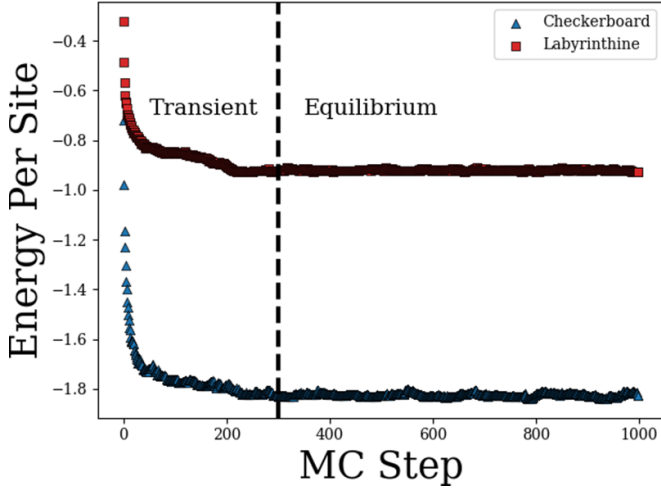
Figure 2. The energy per site as a function of MC step for representative 'checkerboard' (blue triangles) and 'labyrinthine' (red squares) simulations at $k_B T = 1.0$. After 300 MC steps, represented by the dashed vertical line, the system was considered to be in equilibrium.

$$\Delta H^* = \Delta H + \frac{\Delta \mathcal{H}}{2}. \tag{4}$$

The rate associated with a hop from configuration C_i to configuration C_j was then determined according to equation (5) where r_{ij} is the rate, ν is the attempt frequency which we have chosen as 10^{12} Hz, ΔH^* is the energy barrier for the transition, and T is the simulation temperature

$$r_{ij} = \nu \exp\left(-\frac{\Delta H_i^*}{k_B T}\right). \tag{5}$$

The rate catalogue was then constructed according to equation (6) where R_j is the jth element of the rate catalogue. Selection of an event is carried out by taking the product of a random number $u_2(0,1)$ and the total rate R_N and then performing a binary search to find the element R_n of the rate catalogue such that $R_{n-1} < u_2 R_N < R_n$. Afterwards, the configuration is updated to C_n and the simulation time is increased according to equation (7) where $u_3(0,1)$ is a random number uncorrelated with u_2. Using this approach, each element of the rate catalogue has a probability of being selected that is proportional to the rate at which the event occurs

$$R_j = \sum_{j=1}^{N} r_{ij} \tag{6}$$

$$\Delta t = R_N^{-1} \ln \frac{1}{u_3}. \tag{7}$$

For each kMC simulation a MC simulation was first conducted using the methodology described above. The final configuration of the MC simulation was used as the initial state of the kMC simulation. Each kMC simulation was allowed 1000 kMC steps where a single kMC step would be comprised of N diffusion events, i.e. time steps, where $N = 900$ is the number of sites in the simulation.

2.3. Diffusivity calculations

The tracer diffusivity, D_T can be calculated from the mean squared displacement (MSD) of atoms over the course of the simulation according to equation (8) where D_t is the tracer diffusivity, n is the number of spatial dimensions, and t is the simulation time [17]

$$D_T = \lim_{t \to \infty} \frac{\text{MSD}}{2nt}. \tag{8}$$

The temperature and composition dependence of the tracer diffusivity can then be further described as,

$$D_T(\chi, T) = \frac{a^2}{n} \Gamma(\chi, T) f_T(\chi, T) \tag{9}$$

where $f_T(\chi, T)$ is the hop correlation factor, a is the nearest-neighbor hop distance, and $\Gamma(\chi, T)$ is the average single-particle jump rate [48]. The correlation factor, $f_T(\chi, T)$ contains the so-called 'memory effects' that arise as a result of correlated hops. The correlation factor can be determined from simulations by considering the relationship the average number of hops as shown in equation (10) [48]

$$f_T = \frac{\text{MSD}}{a^2 \langle N_h \rangle}. \tag{10}$$

Frequently, the diffusivity can be described by an Arrhenius relationship defined by equation (11), where D_0 is the diffusivity prefactor and Q is the apparent activation energy. When diffusivity is plotted against inverse temperature on a semi-log plot, these quantities are related to the intercept and slope respectively. Over the course of our kMC simulations, the MSD and time were stored and used to fit the diffusivity using the least-squares method and compute the correlation factor

$$D_T = D_0 \exp\left(-\frac{Q}{k_B T}\right). \tag{11}$$

2.4. Order parameters

To quantify the degree of ordering in our simulations, we have elected to use the Warren–Cowley [58, 59] SRO parameters $\alpha^{(n)}$ defined according to equation (12) where n corresponds to the neighbor shell. For example, $\alpha^{(1)}$ would correspond to an SRO defined by nearest-neighbor bonds. Here, $p_{ij}^{(n)}$ is the average fraction of unlike bonds in the nth shell of an atom and χ_A and χ_{Va} are the atomic fraction of atoms and vacancies respectively

$$\alpha^{(n)} = 1 - \frac{p_{ij}^{(n)}}{2\chi_A \chi_{Va}}. \tag{12}$$

LRO was described using the parameter ζ [60] defined according to equation (13) where r_A is the fraction of sites that are correctly occupied by atoms when compared to the ground state, i.e. the ordered 'checkerboard' structure that the simulation is initialized in

$$\zeta \equiv \frac{r_A - \chi_A}{1 - \chi_A}. \tag{13}$$
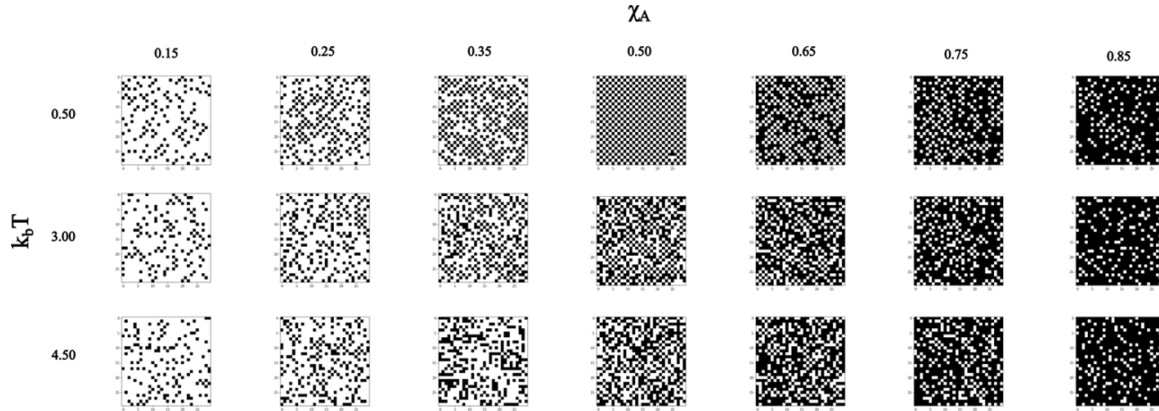
4

Figure 3. The simulation structure generated by a Monte Carlo simulation of 1000 steps with energetics calculated according to equation (1). At low temperature there are substantial ordered domains of the 'checkerboard' structure are present, especially at $\chi_A = 0.50$ wherein the entire simulation has ordered except for a single site. At the intermediate temperature much of the short-range order is lost except for some small ordered domains present at $\chi_A = 0.35$, $\chi_A = 0.50$, $\chi_A = 0.65$. At high temperatures the ordering has disappeared.

3. Results and discussion

3.1. 'Checkerboard' structure

The simulation structures after 1000 MC steps using the checkboard Hamiltonian are shown as a function of temperature and composition in figure 3. Here, vacancies are shown as black and atoms as white. At the lowest temperature, ordered domains are seen at all compositions except $\chi_A = 0.15$ and $\chi_A = 0.85$. At the $\chi_A = 0.50$ composition the whole simulation domain has ordered with the exception of single site. At the intermediate temperature, the degree of ordering is much lower, though some small ordered domains remain for the $\chi_A = 0.35$, $\chi_A = 0.50$, and $\chi_A = 0.65$ compositions. Unsurprisingly, the most substantial ordering remains present at the $\chi_A = 0.50$ composition. At high temperatures virtually no ordered domains are present.

To better understand the effects of temperature and composition on short range order in this system, we have plotted the Warren–Crowley parameters for the first, second, and third nearest neighbors as a function of temperature for several different compositions. Figure 4 shows that in the low temperature limit for the $\chi_A = 0.50$ composition $\alpha^{(1)} \to -1$, indicating the presence of unlike spins in the nearest neighbor shell whereas $\alpha^{(2)} \to 1$ and $\alpha^{(3)} \to 1$ indicating the presence of alike spins in the second and third neighbor shells respectively. Of course, these are expected results since the Hamiltonian was chosen in order to construct the 'checkerboard' structure by penalizing same type nearest neighbor bonds. In the high temperature limit, all of the Warren–Crowley parameters trend towards zero as expected for a random solution.

The diffusivity and first nearest neighbor SRO parameter $\alpha^{(1)}$ in the kMC simulations are plotted in figure 5(a) as a function of temperature for compositions ranging from $\chi_A = 0.15$ to $\chi_A = 0.85$. At high temperatures, the alloy is disordered and the slope of the diffusivity, i.e. the apparent activation energy, appears to be roughly the same for all compositions.

However, in the low temperature limit, several compositions exhibit changes in apparent activation energy, with the most dramatic change at the $\chi = 0.50$ composition where there is a significant increase. Interestingly, this composition also possesses the greatest degree of SRO as $\alpha^{(1)} \to -1$.

Figure 5(b) shows the diffusivity and SRO results obtained as a function of composition at temperatures ranging from $k_B T = 1.5$ to $k_B T = 3.0$. Examination of the trends in $\alpha^{(1)}$ reveal that for all of the temperatures sampled there is a peak in the SRO corresponding to the $\chi = 0.50$ composition. Furthermore, this peak is associated with local minima in the diffusivity at the same composition for $k_B T = 1.5$ and $k_B T = 2.0$, but no minima are present at the higher temperatures sampled. Additionally, we see that $\alpha^{(1)} > 0.80$ at the $\chi = 0.50$ composition for the two curves that display local diffusivity minima, whereas $\alpha^{(1)} < 0.5$ for the curves that do not. Furthermore, we note that the asymmetry of the tracer diffusivity about $\chi_A = 0.50$ is due to the availability of adjacent vacancies for atoms to hop to changing as a function of vacancy concentration.

Figure 6(a) shows the diffusivity (blue circles), SRO (red squares), LRO (green diamonds), and correlation factor (purple triangles) data at the $\chi_A = 0.50$ composition as a function of temperature. The black dashed lines indicate a bilinear fit to the diffusivity data. The range of the two linear fits and their intersection was determined by plotting the sum of the residuals for both fits as points were added from one linear fit and removed from the other, and then selecting the partition that minimized the sum of the square of the residuals. The intersection of these two lines then determines the temperature where the diffusivity transitions from a high to low apparent activation energy. Using this method, the transition temperature was determined to be $k_B T_{\text{trans}} = 2.89$ and is shown as a dashed vertical line in figure 6(a).

Examination of figure 6(a) reveals several interesting insights. First, the transition from low to high apparent activation energy was determined to be $k_B T = 2.89$, whereas the
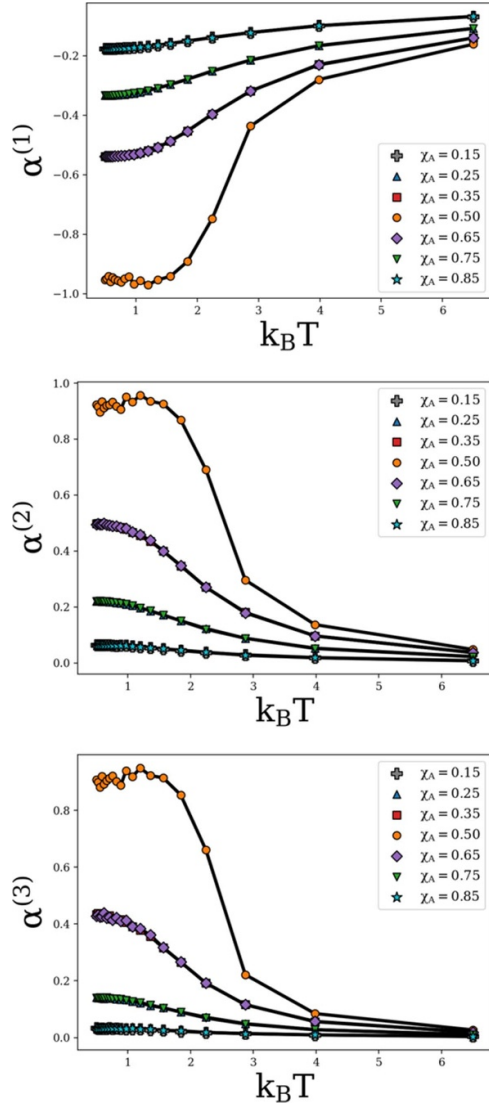
Figure 4. The SRO parameters determined by averaging the SRO parameters from the last 100 Monte Carlo steps of each simulation for simulations conducted with the Hamiltonian shown in equation (1). Here, we can see that at low temperatures $\alpha^{(1)} \rightarrow -1$ indicating the presence of unlike spins in the nearest neighbor shell whereas $\alpha^{(2)} \rightarrow 1$ and $\alpha^{(3)} \rightarrow 1$ indicating the presence of alike spins in the second and third neighbor shells respectively.

LRO transition temperature appears to be $k_{\mathrm{B}}T \sim 2.26$, which is consistent with Onsager's solution for the order-disorder transition of the two-dimensional Ising model [61]. Second, the correlation factor f_{T} is shown to smoothly decrease as the magnitude of SRO increases, even in the temperature regime where $\zeta = 0$, suggesting that hop correlation factor is more closely related to SRO than LRO. Figure 6(b) plots the correlation factor as a function of the magnitude of SRO and reveals a power-law relationship between the quantities with an exponent of roughly 2.30. Finally, figure 6(a) also shows that the change in apparent activation energy is substantial, with the low temperature apparent activation energy being nearly twice that of the high temperature. At first, this seems surprising, especially considering that the low temperature

apparent activation energy is greater than the energy barrier for any single hop present in the kMC simulation. However, this can all be rationalized by a detailed understanding of the energetics of diffusion and the contribution of memory effects.

3.2. The four-step diffusion mechanism and memory effects

To determine the mechanism causing the high apparent activation energy, we first looked at the distribution of energy barriers associated with successful jumps from our kMC simulations. Examples of such distributions for temperatures above and below the change in slope are shown in figures 7(a) and (b) respectively. These distributions were generated by creating histogram of energy barriers found in the simulation, sampled at the end of each kMC step and normalized such that the distribution sums to unity. For simulations run at temperatures above the change in slope, the energy barriers are approximately normally distributed about $\Delta H = 15c$, which the reader may recall was the direction-independent energy barrier that we selected. Of course, this result is to be expected since in disordered configurations a single diffusion event should be equally likely to result in an increase or decrease in energy. In the low temperature case, the distribution is seen to be effectively bimodal with the most common barriers being the smallest and the largest present in the simulation. This suggests that, in the ordered state, the majority of diffusion events consist of and atom hopping out of the ordered state—an event that would have the greatest activation energy—and then immediately hopping back into the ordered state due to the energetic preference and low activation barrier associated with a transition into the low energy ordered state.

To completely understand the large apparent activation energy shown at low temperatures in figure 6(a), we first need to understand how diffusion occurs in the ordered checkboard structure. That is to say, when there is no intercalating network of vacancies for the atom to diffuse through, what is the simplest way to achieve net diffusion? Figure 8 depicts the simplest mechanism that results in two second nearest neighbor atoms switching places and thereby producing net diffusion via a four-step mechanism.

To determine the apparent activation energy of this mechanism, we performed a constrained kMC simulation on a 4×4 square lattice with an initial state as shown in the first step of figure 8. The sites on the perimeter of the simulation cell were constrained such that no atoms on the perimeter were allowed to move, i.e. the only diffusion events available were those that occurred within the center four sites. The tracer 'diffusivity' of our four-step mechanism was then determined by counting the number of times that the atoms in this center square swapped places over the course of the simulation. We note that here the number of swaps refers to the number of times that the two atoms within these constrained kMC simulations swap places and is not the same as the number of times that an atom and vacancy swap places. Following the standard procedure, we were then able to extract the apparent activation energy associated with this mechanism by fitting the slope of the Arrhenius
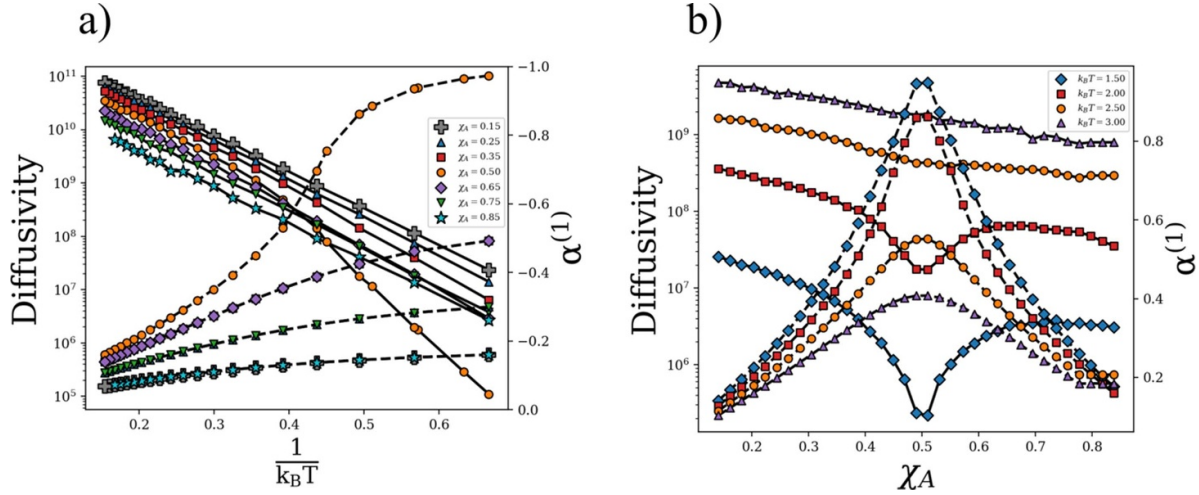
Figure 5. (a) The tracer diffusivity (solid) and short-range order (dashed) results from kMC simulations conducted using the Hamiltonian in equation (1) and SRO parameter in equation (10) as a function of temperature. The plot demonstrates that at the $\chi_A = 0.50$ composition a rapid increase in short-range order is associated with a decline in diffusivity. (b) The tracer diffusivity (solid) and short-range order (dashed) results from kMC simulations conducted using the Hamiltonian in equation (1) and SRO parameter in equation (10) as a function of composition. It can be seen that diffusivity minima correspond to SRO maxima at the $\chi_A = 0.50$ composition.
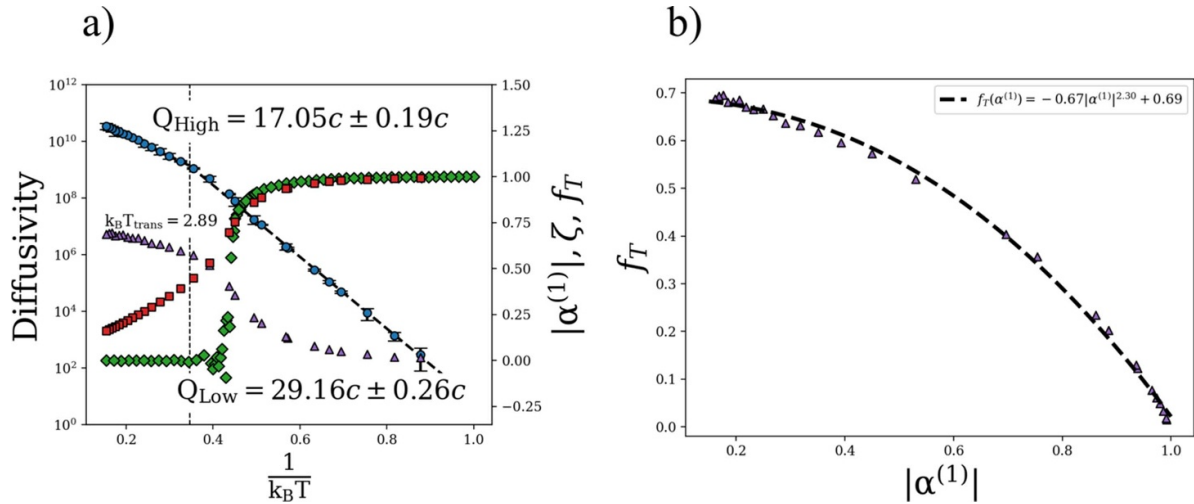

Figure 6. (a) The tracer diffusivity (blue circles), SRO, $\alpha^{(1)}$, (red squares), LRO, ζ, (green diamonds) and correlation factor, f_T (purple triangles), of the $\chi_A = 0.50$ composition as a function of temperature as determined from kMC simulations. The black dashed lines indicate the linear fits to each section of data. A dashed vertical line indicates the transition temperature $k_B T_{\text{trans}} = 2.89$ at which the apparent activation energy is seen to increase. The apparent activation energies obtained from these fits are $Q_{\text{High}} = 17.05c \pm 0.19c$ and $Q_{\text{Low}} = 29.16c \pm 0.26c$ for the high temperature and low temperature respectively. (b) The calculated correlation factor, f_T, plotted with respect to the absolute value of SRO, $\alpha^{(1)}$. The dashed line indicates a power-law fit to the relationship between f_T and $|\alpha^{(1)}|$.

plot. This plot as well as the distribution of energy barriers over the course of the constrained simulation are shown in figures 9(a) and (b), respectively. These results provide two interesting insights into the low-temperature behavior presented in figures 5 and 6. First, the apparent activation energy of the four-step mechanism was found to be $Q = 28.74c$, which is larger than any individual energy barrier present in the simulation, just as was found in the low-temperature behavior of the larger scale kMC simulations shown in figure 6(a). This result is encouraging because it provides support that the mechanism for net diffusion in our larger scale kMC simulations is indeed comprised of a multi-step process involving correlated hops.

The energy barrier distributions shown in figure 9(b) are also quite similar to the low temperature distributions shown in figure 7(b). The most significant feature of both distributions is the fact that the most common events are the lowest and highest energy barriers present in the system. The prevalence of these energy barriers suggests that at low temperatures the atoms spend most of their time hopping the states shown in steps 1 and 2 in figure 8. Hopping from step 1–2 requires the atom to go from a state in which all four of its nearest neighbors are vacancies, which is the most favorable state, into a state in which three of the four of its nearest neighbors are atoms, which is an energetically unfavorable state due
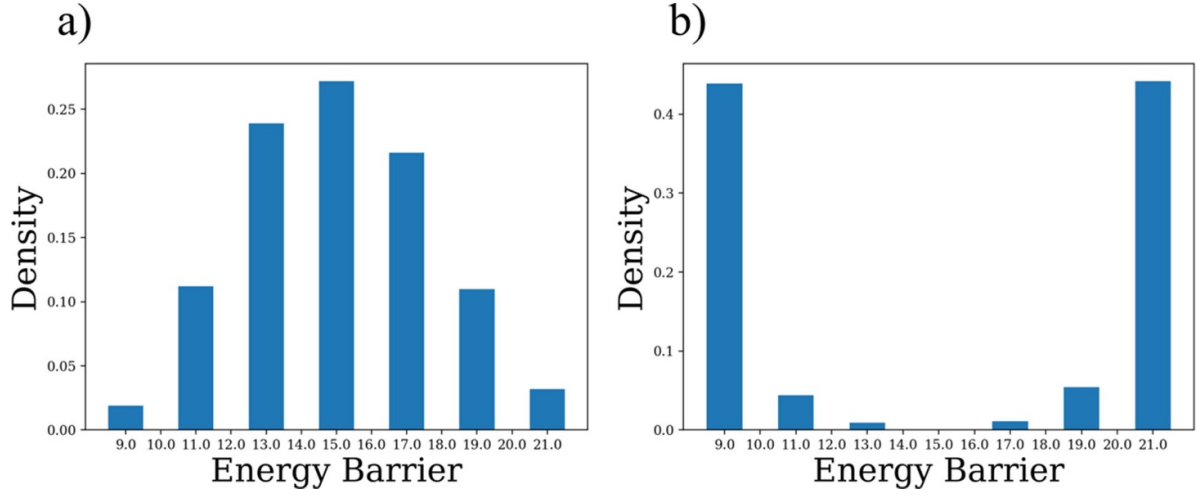
Figure 7. (a) The distribution of energy barriers generated by kMC simulations at a temperature of $k_B T = 6.5$ using the Hamiltonian defined in equation (1). The barriers were sampled at each 'kMC step' as previously defined for a total of 1000 samples per simulation. The energy barriers appear to be approximately normally distributed around $15c$. (b) The distribution of energy barriers generated at a temperature of $k_B T = 1.5$ using the Hamiltonian defined in equation (1). The distribution is approximately bimodal with the most common energy barriers being the smallest and largest possible in the simulation.
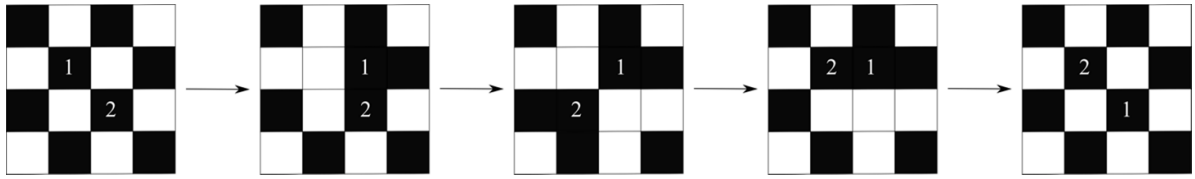

Figure 8. A schematic representing one mechanism by which net diffusion can occur in the ordered 'checkerboard' structure. The mechanism requires at least four hops after which two second nearest neighbor atoms swap places. The black squares represent atoms, and the white squares represent structural vacancies.
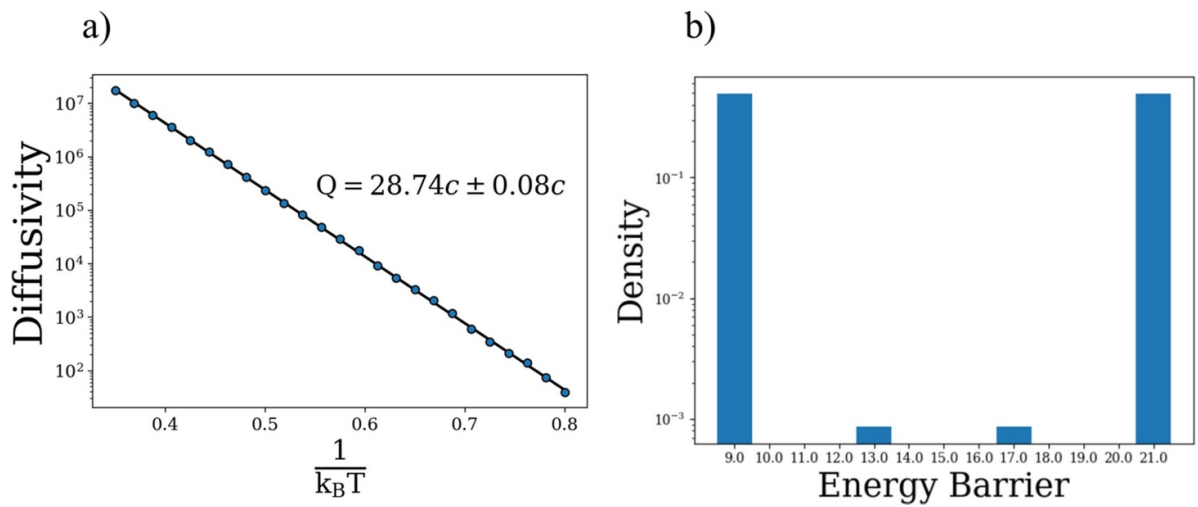

Figure 9. (a) The Arrhenius plot constructed from the constrained kMC simulation representing the four-step mechanism. The apparent activation energy determined from fitting the slop was found to be $Q = 28.74c \pm 0.08c$, which is higher than any of the individual energy barriers present in the simulation. (b) The distribution of energy barriers present in the constrained four-hop simulation. The most common energy barriers are the smallest and largest present in the system.
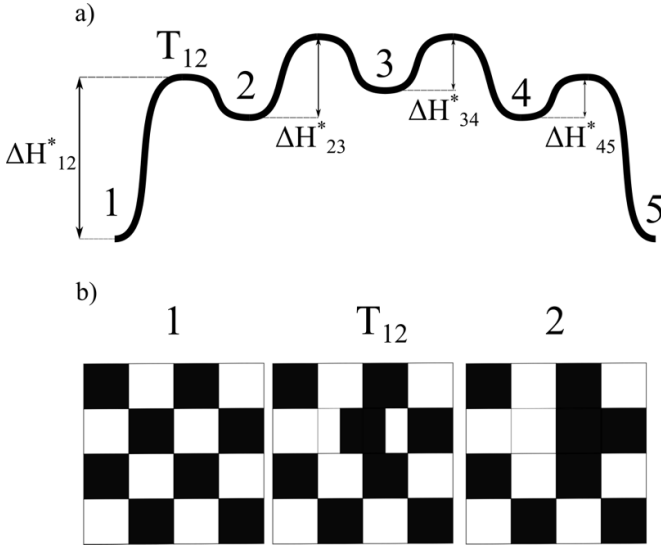
8

a)

b)

Figure 10. (a) A schematic representation of the potential energy landscape throughout the four-step process. Each equilibrium position is labelled 1–5 corresponding to the configurations in figure 8. The label T_{12} indicates the transition state between configurations 1 and 2. We note that using the Brønsted–Evans–Polanyi principle, all of the transition states have the same energy; however, under our analytical model this assumption is relaxed. The energy barriers between each position are labelled and correspond to the four energy barriers present in the distribution in figure 9(b). (b) The configuration of atoms at at the equilibrium and transition positions during the hop from 1 to 2.

to same-type neighbors. Though the least energetically favorable state would be for an atom to have four same-type nearest neighbors, the situation described here actually represents the largest and smallest energy barriers when determined according to equation (4). This is because it is not possible for an atom to go from the lowest energy state to the highest energy state in a single jump due to the necessity for an atom to swap places with a neighboring vacancy in order for diffusion to occur. Thus, any diffusion event must result in the diffusing atom having at least one neighboring vacancy before and after the hop.

The kMC results demonstrate that indeed the apparent activation energy for diffusion is higher than any individual event at low temperatures, which must be a result of correlated events. As noted in [48–50], the apparent activation energy can be split into contributions from the total hop rate and the correlational effects: $Q = Q_{\text{corr}} + Q_{\text{hop}}$. At low temperatures, following [48–50], the total Q_{hop} is the largest barrier, here $21c$, and so that the Q_{corr} approximately $8c$. While this approach provides an understanding of the additional energy barrier and its origins, it is unable to concretely quantify the activation energies without direct simulations.

Here, we take an alternative approach by considering a five-state random walk as illustrated in figure 10(a), an atom must hop across four energy barriers successfully and each in succession. The probability of the atom in state n at time t is $P(n,t)$ and the initial condition is $P(n,0) = \delta_{n1}$. Because the transition rates between consecutive states are known and the new walk depends on previous walks, the evolution of $P(n,t)$ can

be expressed in a Markov chain where the transition matrix is as follows:

$$
\frac{dP(n,t)}{dt} = r_{n-1\to n}P(n-1,t) + r_{n+1\to n}P(n+1,t)
$$
$$
- (r_{n\to n-1} + r_{n\to n+1})P(n,t). \tag{14}
$$

The physical meaning of equation (14) is the probability rate of change equals the net flux, where $r_{n-1\to n} = \nu \exp(-\Delta H_{n-1\to n}/k_{\text{B}}T)$ is the rate for walking from the state $n-1$ to n. After obtaining $P(n,t)$ from equation (14), the net rate to reach state 5 can be computed as $r_{4\to 5}P(4,t)$. Though the analytic solution of $P(n,t)$ does not exist, we can approximate the arrival time by the exponential distribution (Poisson's process) and obtain the apparent activation energy at low-temperature and high-temperature limits (with details covered in appendix). In our approximate model, the net jump time from state 1–5 is the sum of the time for all possible net jumps from the state $n-1$ to n where $n \leqslant 5$. At high temperatures, the apparent activation energy is

$$
\Delta H
$$
$$
= \frac{4\Delta H_{12}^* - 3\Delta H_{21}^* + 6\Delta H_{23}^* - 4\Delta H_{32}^* + 6\Delta H_{34}^* - 3\Delta H_{43}^* + 4\Delta H_{45}^*}{10}. \tag{15}
$$

And at low temperatures, the apparent activation energy in our example is

$$
\Delta H = \Delta H_{12}^* + \Delta H_{23}^* - \Delta H_{21}^*, \tag{16}
$$

which makes intuitive sense since it is simply the energy level of the highest transition state in the sequence of hops.

Inserting the values from the energy barrier distribution in figure 9(b), $\Delta H_{12}^* = \Delta H_{54}^* = 21c$, $\Delta H_{23}^* = \Delta H_{43}^* = 17c$, $\Delta H_{34}^* = \Delta H_{32}^* = 13c$, and $\Delta H_{45}^* = \Delta H_{21}^* = 9c$, we find that the apparent activation energy is $29.0c$ in the low-temperature limit and $17.0c$ in the high-temperature limit. The analytical value at low temperatures compares well with the results of the constrained kMC simulation shown in figure 9(a), indicating a match between our analytical theory and constrained kMC. Additionally, the apparent activation energies from our four-step mechanism are within one standard deviation of error of the result determined from the large-scale kMC in both low temperatures and high temperatures shown in figure 6. Due to the agreement of the apparent activation energies across our low temperature large-scale kMC, constrained kMC, and approximate model, we conclude that the mechanism for net diffusion present in the low temperature large-scale kMC is the proposed four-step mechanism. This, in turn, provides a reasonable explanation for the relationship between the increase in SRO and the increase in activation energy, since the four-step mechanism assumes that the diffusion is constrained by a preference to retain SRO which leads to additional correlational effects on the tracer diffusivity.
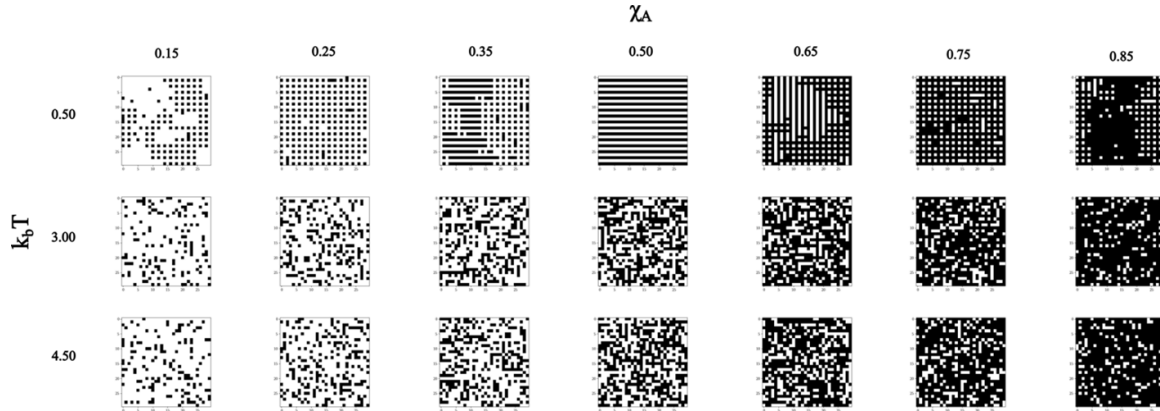
Figure 11. The simulation structures generated by Monte Carlo simulations of 1000 steps with energetics calculated according to equation (2). At low temperature there are substantial ordered domains of the 'labyrinthine' structure are present, especially at $\chi_A = 0.50$ wherein the entire simulation has ordered in a single direction along the x-axis. The other compositions depict a 'hatch' type of structure. At the intermediate and high temperatures most of the short-range order is lost.

3.3. 'Labyrinthine' structure

The simulation structures after 1000 MC steps with energetics calculated according to equation (2) are shown as a function of temperature and composition in figure 11. As with the structures generated by the Hamiltonian in equation (1), the structures become disordered as the simulation temperature is increased with only small ordered regions present at $k_B T = 3.00$ and virtually random arrangements at $k_B T = 4.50$. At the lowest temperature, two distinct types of ordering are present. The first and most obvious is shown at the $\chi_A = 0.50$ composition in which the entire simulation domain has ordered into stripes along the *x*-axis. This structure is what we have called the 'Labyrinthine' structure in figure 1 because of the appearance of the structure being reminiscent of a labyrinth when many ordered domains of different orientation are present. The second structure is the 'hatch' structure which is most prominent at the $\chi_A = 0.25$ and $\chi_A = 0.75$ compositions, though small domains are present at all compositions with the exception of $\chi_A = 0.50$.

The SRO parameters are shown in figure 12. In contrast to the results from the 'checkerboard' simulations, we see very little ordering of the first-nearest neighbors, with the exception of the $\chi_A = 0.25$ and $\chi_A = 0.75$ compositions for which $\alpha^{(1)} \to -0.25$ at low temperatures, corresponding to ordering in the 'hatch' structure. Of course, the lack of strong nearest neighbor interactions is expected since the Hamiltonian in equation (2) is only written in terms of second and third nearest neighbor interactions. As a consequence, figure 12 shows $\alpha^{(2)} \to -1.0$ and $\alpha^{(3)} \to 1.0$ for the $\chi_A = 0.50$ composition at low temperatures. $\alpha^{(3)}$ indicates low-temperature attraction between same-type third nearest neighbors for all of the compositions sampled. This suggests that the third nearest neighbor interactions may dominate in forming the 'hatch' structure whereas the 'labyrinthine' structure requires both repulsion of second nearest neighbors and attraction of third nearest neighbors. In fact, $\alpha^{(3)} \to 1$ at low temperature for all of the

compositions sampled. This is because at low temperatures all compositions show some degree of ordering.

Figure 13 plots the diffusivities and SRO results obtained from kMC simulations as a function of temperature and composition for simulations run with Hamiltonian 2. As before, we see that there is an increase in apparent activation energy (slope) associated with the rising SRO. Most apparently, the $\chi_A = 0.50$ composition appears have the largest increase in its activation energy as well as the most SRO. At low temperatures, figure 13(b) indicates that there are multiple minima in diffusivity with respect to composition. These minima also appear to correspond to peaks in the SRO at the $\chi = 0.25$, $\chi = 0.50$, and $\chi = 0.75$ compositions and thus correspond to the ordered low energy 'labyrinthine' and 'hatch' structures.

Figure 14(a) shows the tracer diffusivity, SRO, and correlation factor as a function of inverse temperature for the $\chi_A = 0.50$ composition as this state has the largest change in diffusivity. There is a notable change in the diffusivity slope on the semilog plot at $k_B T_{\text{trans}} = 2.27$. The value of the SRO parameter $\alpha^{(3)}$ at this temperature was roughly 0.16. In contrast to the 'checkboard' structure, the magnitude of the change in slope is lower and there is a lesser degree of SRO at the transition temperature.

Figure 14(b) depicts the correlation factor as a function of $\alpha^{(3)}$. The figure shows that for the 'labyrinthine' structure, as was also seen in the 'checkerboard' structure, there is a power-low type relationship between the correlation factor and SRO with an exponent of roughly 2.30. In the case of the 'labyrinthine' structure; however, the power-law fit contains a smaller leading coefficient which may be due to the fact that the ordering of the 'labyrinthine' structure contains a larger network of connected diffusion when compared to the 'checkerboard' structure that has very few connected vacancies.

The energy barrier distributions for the simulations conducted above and below the transition temperature, at $k_B T = 6.50$ and $k_B T = 0.71$, are plotted in 15a and 15b respectively. The energy barrier distribution shown in figure 15(a)
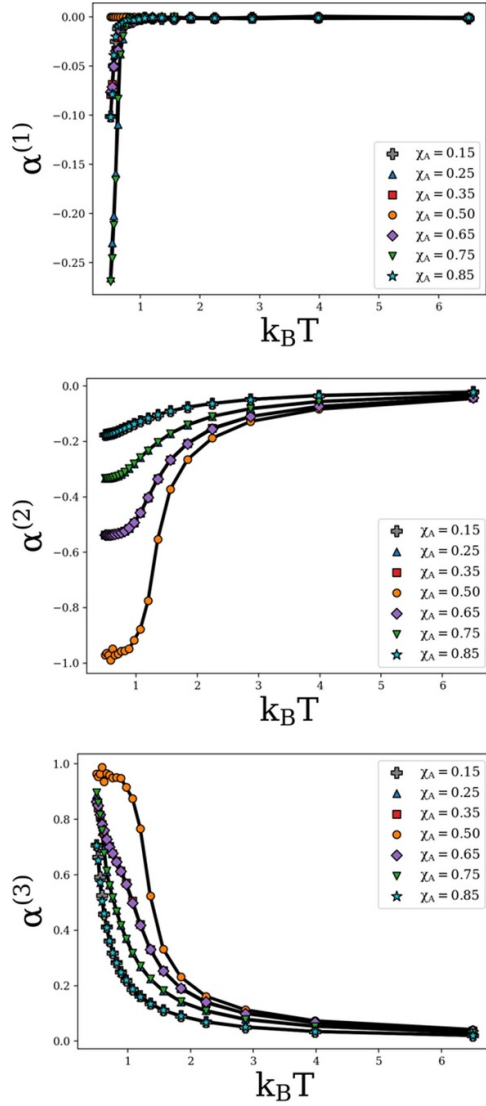
Figure 12. The SRO parameters determined by averaging the SRO parameters from the last 100 Monte Carlo steps of each simulation for simulations conducted with the Hamiltonian shown in equation (2).

strongly resembles that of figure 6(a), wherein the energy barriers are normally distributed around $15c$. However, we note a major difference in the low-temperature distribution, shown in figure 15(b), between the ordered 'labyrinthine' structure and the 'checkerboard' structure. As opposed to the bimodal distribution observed for the 'checkerboard,' the distribution for the 'labyrinthine' structure is trimodal with the most common energy barrier being $15c$. In the 'labyrinthine' structure, this energy barrier is also associated with diffusion down a row of vacancies, since the local environment is constant for an atom diffusing anywhere along a vacant row. According to our earlier idea that these vacant rows would act as high-diffusivity pathways, this energy barrier would be most common. The

other two peaks are associated with the largest changes in energy available for a single jump given that the energetics are determined by equation (2). As we saw in the 'checkerboard' structure, the high frequency of occurrence of these barriers is likely due to an atom jumping into and out of the ordered structure repeatedly before any net diffusion occurs. Thus, in the 'labyrinthine' structure, diffusion likely occurs by an atom jumping into and out of the low energy ordered structure repeatedly until it escapes its initial local environment. Once the atom has distanced itself from the initial local environment, a net displacement is achieved via diffusion along a string of vacancies acting as a high-diffusivity pathway.

Finally, we can use these energy barrier distributions as inputs in our approximate solution shown in equations (15) and (16) to estimate the apparent activation energy for a 4-step diffusion event as we did with the 'checkerboard' structure. A schematic of this diffusion process is shown in figure 16. Although the approximate model was constructed in order to represent the 4-step mechanism described previously, it can be applied here to describe a scenario in which an atom jumps out of the ordered 'labyrinthine' structure and into a row of vacancies. The atom then completes two jumps within the row of vacancies before it is able to jump back into the ordered structure, though in the larger scale simulations it is likely that the diffusing atom jumps along the row of vacancies many times before it is able to jump back into the ordered structure.

To describe this situation, we use $\Delta H_{12}^* = 19c$, $\Delta H_{23}^* = \Delta H_{34}^* = 15c$, and $\Delta H_{45}^* = 11c$, as inputs to the model, since, within the row of vacancies, the energy barrier is $15c$. Given these inputs, the apparent activation energy at high temperature is $16.2c$ which is close to kMC results. However, the apparent activation energy at low temperatures from equation (14) gives $Q = 23c$, which is somewhat larger than the apparent activation energy determined from our fit of the kMC data. According to our approximate model in appendix, the apparent activation energy at low-temperature limit can be written in equation (12) only when the activation energy for the net jump $\Delta H_{12}^* + \Delta H_{23}^* - \Delta H_{21}^*$ is much larger than the activation energy for other net jumps. In this case, there are two net jumps with the activation energy $23c$ ($\Delta H_{12}^* + \Delta H_{23}^* - \Delta H_{21}^*$, $\Delta H_{12}^* + \Delta H_{23}^* + \Delta H_{34}^* - \Delta H_{32}^* - \Delta H_{21}^*$). This would then explain the large modes of energy barriers $11k_B$, $15k_B$, and $19k_B$ in figure 15(b), which are associated with the back-and-forth jumps (ΔH_{12}^*, ΔH_{21}^*) and (ΔH_{23}^*, ΔH_{32}^*). We also notice that the activation energy of the net jump $\Delta H_{12}^* = 19c$ which is much less than $23c$ and therefore the approximate model has less accuracy, presumably because the actual diffusion process here contains more than four jumps. In this case, it would be more accurate to use the rigorous solution from equation (12) to obtain the apparent activation energy at low temperatures. While the approximate model was developed based on a simplified physical process, it is shown to still provide reasonable estimates.
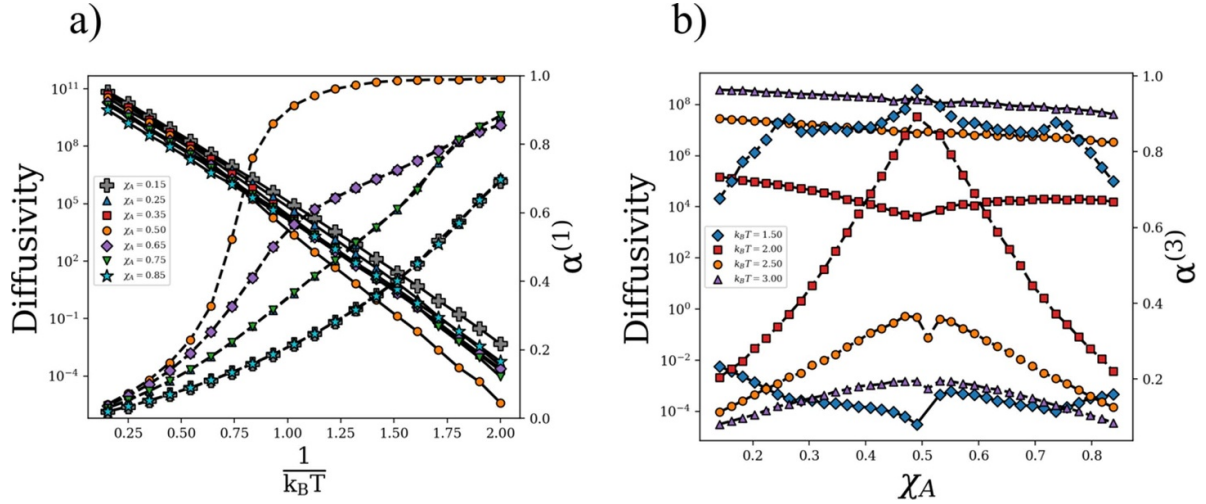
Figure 13. (a) The tracer diffusivity (solid) and short-range order (dashed) results obtained from kMC simulations conducted using the Hamiltonian in equation (2) and SRO parameter in equation (10) as a function of temperature. The results demonstrate the correlation between SRO and a change in diffusion activation energy as the slope of the semi-log plot increases at temperatures below the order-disorder transition. This effect is most apparent for the $\chi_A = 0.50$ composition in which the ordering is strongest and corresponds to the lowest diffusivity at temperatures below the order-disorder transition. (b) The tracer diffusivity and SRO as a function of composition. Here, we can see that for the $k_B T = 1.50$ curve there are three maxima in SRO corresponding to the onset of the 'hatch' structures at $\chi_A = 0.25$ and $\chi_A = 0.75$ compositions as well as the 'labyrinthine' structure at $\chi_A = 0.50$. Here, we can see that this corresponds to minima in diffusivity at $\chi_A = 0.50$ and $\chi_A = 0.75$. As the temperature increases, less ordering was evident as the diffusivity curves become essentially linear because of the compositional dependence of the diffusivity prefactor.
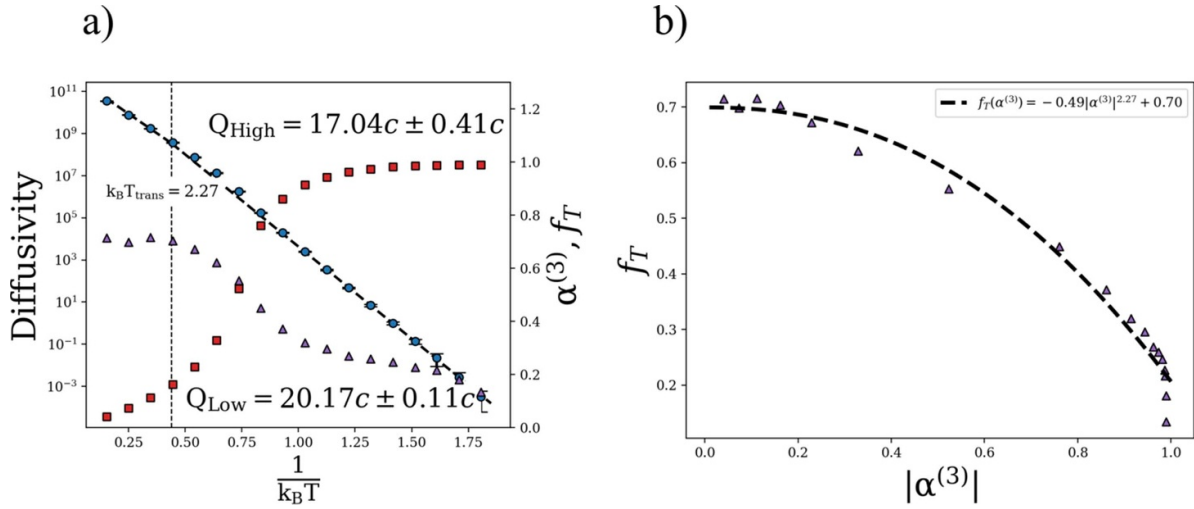

Figure 14. (a) The tracer diffusivity (blue circles), SRO, $\alpha^{(3)}$, (red squares), and correlation factor, f_T (purple triangle), for the kMC simulations run with the Hamiltonian in equation (2) at $\chi = 0.50$. As was seen before with the first Hamiltonian, there is a slight change in apparent activation energy (slope) at $k_B T = 2.27$. In contrast with the 'checkerboard' structure, the 'labyrinthine' structure has a much less significant change in slope. The value of $\alpha^{(3)}$ at the transition was roughly 0.16. (b) The calculated correlation factor, f_T, plotted with respect to the absolute value of SRO, $\alpha^{(3)}$. The dashed line indicates a power-law fit to the relationship between f_T and $|\alpha^{(3)}|$.
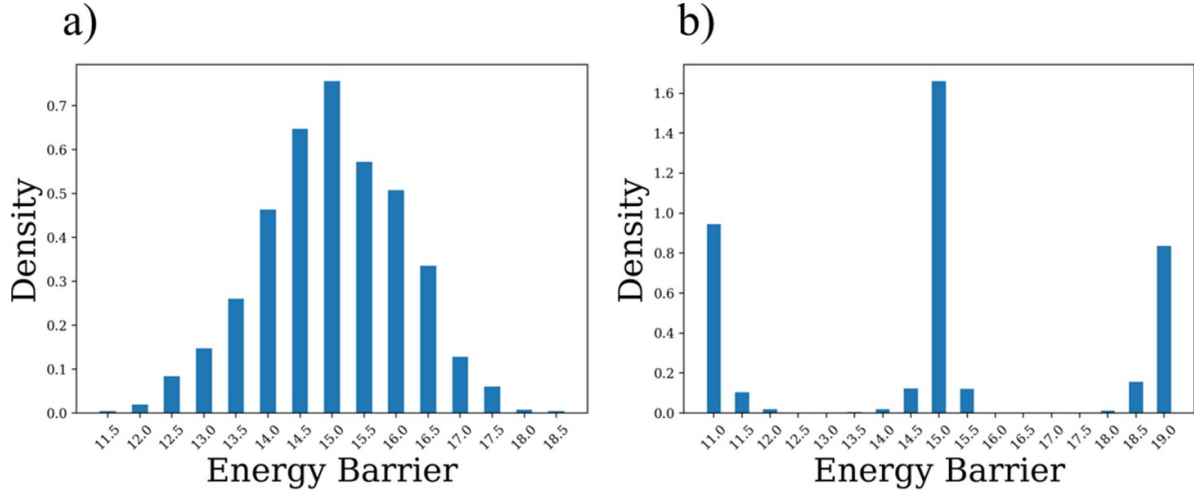
Figure 15. (a) The distribution of single-hop energy barriers present in a kMC simulation conducted at $k_B T = 6.5$ with energetics according to equation (2). The energy barriers are approximately normally distributed around $15c$, which is associated with a hop with no net change in energy. (b) The distribution of single-hop energy barriers present in a kMC simulation conducted at $k_B T = 0.71$. The energy barriers are distributed approximately trimodally, with the most frequent jumps being those with no net energy change as well as the jumps associated with the greatest changes in energy.
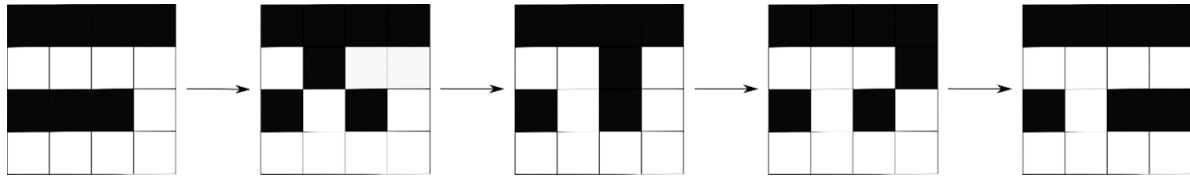

Figure 16. A schematic representing the configurations described by the application of our approximate model to diffusion along a row of vacancies in the ordered 'Labyrinthine' structure. The atom (black) begins by jumping into a row of vacancies (white) followed by two hops along the row and then a final jump back into the row of atoms, though it should be noted here that the ordered structure is imperfect due to the presence of an additional vacancy in the row of atoms. In a large-scale simulation, it is likely that many more jumps along the row of vacancies would occur before the atom is able to jump back into the row of atoms.

4. Summary and conclusions

In this work, we have used MC and Kinetic MC simulations on a square lattice in order to investigate the influence of vacancy ordering on diffusion. We examined two different energetic scenarios that produced three different ordered structures. In the first case, the ordered 'checkerboard' phase formed near $\chi_A = 0.50$ because of the energetic penalty for like-type nearest neighbors in Hamiltonian 1. In the second case, two ordered structures formed: the 'hatch' structure at the $\chi_A = 0.25$ and $\chi_A = 0.75$ compositions and the 'labyrinthine' structure at $\chi_A = 0.50$. These structures developed as a result of repulsive interactions between like second nearest neighbor sites and attraction between like third nearest neighbor sites.

The degree of SRO was quantified using the Warren–Cowley ordering parameters for the first, second, and third nearest neighbors. We found that for each case the apparent activation energy for tracer diffusion was larger in structures that had a high degree of SRO when compared to the disordered structures. This was then concretely demonstrated by analysis of the correlation factor, which was determined to have a power-law relationship with SRO in both the 'checkboard' and 'labyrinthine' structures. In each case, the power-law exponent was roughly 2.30 whereas the leading coefficient's magnitude was greater for the 'checkerboard' structure, suggesting that the strength of the relationship between hop correlation factor and SRO depends on the extent of vacancy networks available in the ordered structure. This is supported by the fact that the 'labyrinthine' structure, which contains strings of vacancies that may act as high diffusivity pathways, possesses a weaker relationship between hop correlation factor and SRO than the 'checkboard' structure that has no interconnected vacancies.

In our examination of the effects of concentration on diffusivity, we found that minima in diffusivity corresponded to maxima in SRO parameters. This again suggests that as SRO increases diffusivity is hindered due to memory effects contained within the hop correlation factor.

To explain the mechanism for orderings effect on tracer diffusion, we constructed an analytical model based on kinetics theory. Our results suggest ordering inhibits diffusion, even when 'high diffusivity pathways' are present, because the rate-limiting step in the kinetic process becomes escaping the local environment of an energetic minima. This step consists of a diffusing atom or vacancy jumping in and out of a low-energy local configuration repeatedly. This process occurs because of a strong energetic bias for the atom to remain in the ordered configuration. In effect, the ordering acts as 'traps', keeping diffusing atoms stuck in the vicinity of the ordered configuration. We found that this process could result in an apparent activation energy for tracer diffusion that surpasses any individual energy barrier in the diffusive process. We note that the diffusion of dilute species, such as light elements, is likely to be enhanced by the presence of strings of structural vacancies in cases where the diffusing species does not form ordered sublattices. A similar inhibition of diffusion may be achieved in these cases if defects are present to act as low-energy 'traps'; for example, when diffusing hydrogen encounters TiC precipitates in α-iron [62].

Turning our attention to the work of Sarian, whose carbon diffusion anomaly in substoichiometric titanium carbide partially motivated this study, we can make several comments. First, Sarian hypothesized that the change in carbon tracer diffusion activation energy was the result of a vacancy order-disorder transition; though we pointed out that the work of Gusev indicates that the order-disorder transition in titanium carbide occurs at significantly lower temperature than Sarian's anomaly. However, Gusev reports the phase boundaries for LRO, but here we have shown that diffusion is likely more strongly affected by SRO, which typically persists to higher temperatures than LRO. Therefore, the results presented here support Sarian's hypothesis and suggest that the reported change in activation energy was likely a result of a SRO-disorder transition on the carbon sublattice of titanium carbide. This suggests that it is SRO, not LRO, that affects the properties of diffusion and implies that diffusivity can be directly impacted by local SRO in vacancy ordered structures with the greatest impact in structures that have a stronger tendency form SRO.

Data availability statement

Acknowledgments

Appendix. The Activation Energy of the 4-Step Mechanism

From the Poisson distribution, the average time required for a jump to happen is $\tau = \frac{1}{r}$, where r is the jump rate. At the position n, the rate for jumping forward to $n+1$ is $r_{n,n+1}$ and for jumping backward to $n-1$ is $r_{n,n-1}$. The average residence time at the position n is

$$\tau(n) = \frac{1}{r_{n,n+1} + r_{n,n-1}}. \tag{A1}$$

The average time from the position n to $n+1$, noted as $t(n \to n+1)$ is computed in the recursive form because there are two ways from n to $n+1$: $n \to n+1$ and $n \to n-1 \to n \to n+1$

$$t(n \to n+1) = \frac{r_{n,n+1}}{r_{n,n+1} + r_{n,n-1}} \times \tau(n) + \frac{r_{n,n-1}}{r_{n,n+1} + r_{n,n-1}}$$
$$\times \left[\tau(n) + t(n \to n+1) + t(n-1 \to n)\right]. \tag{A2}$$

The term $r_{n,n+1}/(r_{n,n+1} + r_{n,n-1})$ and $r_{n,n-1}/(r_{n,n+1} + r_{n,n-1})$ represent the probability of jumping forward and backward at the position n, respectively.

In our case, substituting $\tau(1) = 1/r_{12}$, $r_{10} = 0$ into the above recursive equation, we get:

$$t(1 \to 2) = \frac{1}{r_{12}}, \, t(2 \to 3) = \frac{1}{r_{23}}\left(1 + \frac{r_{21}}{r_{12}}\right), t(3 \to 4)$$
$$= \frac{1}{r_{34}}\left[1 + \frac{r_{32}}{r_{23}}\left(1 + \frac{r_{21}}{r_{12}}\right)\right] \tag{A3}$$

$$t(4 \to 5) = \frac{1}{r_{45}}\left\{1 + \frac{r_{43}}{r_{34}}\left[1 + \frac{r_{32}}{r_{23}}\left(1 + \frac{r_{21}}{r_{12}}\right)\right]\right\}. \tag{A4}$$

Therefore, the total average time from position 1–5 is $t(1 \to 5) = \sum_{i=1}^{4} t(i \to i+1)$

$$t(1 \to 5) = \left(\frac{1}{r_{12}} + \frac{1}{r_{23}} + \frac{1}{r_{34}} + \frac{1}{r_{45}}\right) + \left(\frac{r_{21}}{r_{12}r_{23}} + \frac{r_{32}}{r_{23}r_{34}} + \frac{r_{43}}{r_{12}r_{23}}\right)$$
$$+ \left(\frac{r_{32}r_{21}}{r_{12}r_{23}r_{34}} + \frac{r_{43}r_{32}}{r_{23}r_{34}r_{45}}\right) + \frac{r_{43}r_{32}r_{21}}{r_{12}r_{23}r_{34}r_{45}}. \tag{A5}$$

The average rate is then $R = 1/t(1 \to 5)$ and we would like to find the average ΔH for $R \propto \exp(-\Delta H/k_B T)$ at high temperature and low temperature limits.

At high temperature, $r_{ij} \approx \nu \left(1 - \Delta H_{ij}/k_B T\right)$, the leading term in R is:

$$R = \frac{\nu}{10}\left(1 - \frac{4\Delta H_{12} - 3\Delta H_{21} + 6\Delta H_{23} - 4\Delta H_{32} + 6\Delta H_{34} - 3\Delta H_{43} + 4\Delta H_{45}}{10 k_B T}\right). \tag{A6}$$

Therefore, the average activation energy at high temperature limit is:

$$\Delta H = \frac{4\Delta H_{12} - 3\Delta H_{21} + 6\Delta H_{23} - 4\Delta H_{32} + 6\Delta H_{34} - 3\Delta H_{43} + 4\Delta H_{45}}{10}. \tag{A7}$$

At low temperature, we rewrite the average time as:

$$t(1 \rightarrow 5) = \frac{1}{\nu}\left(\begin{array}{l} \exp\dfrac{\Delta H_{12}}{k_B T} + \exp\dfrac{\Delta H_{23}}{k_B T} + \exp\dfrac{\Delta H_{34}}{k_B T} + \exp\dfrac{\Delta H_{45}}{k_B T} \\[2mm] + \exp\dfrac{\Delta H_{12} + \Delta H_{23} - \Delta H_{21}}{k_B T} \\[2mm] + \exp\dfrac{\Delta H_{23} + \Delta H_{34} - \Delta H_{32}}{k_B T} + \exp\dfrac{\Delta H_{34} + \Delta H_{45} - \Delta H_{43}}{k_B T} \\[2mm] + \exp\dfrac{\Delta H_{12} + \Delta H_{23} + \Delta H_{34} - \Delta H_{32} - \Delta H_{21}}{k_B T} \\[2mm] + \exp\dfrac{\Delta H_{23} + \Delta H_{34} + \Delta H_{45} - \Delta H_{43} - \Delta H_{32}}{k_B T} \\[2mm] + \exp\dfrac{\Delta H_{12} + \Delta H_{23} + \Delta H_{34} + \Delta H_{45} - \Delta H_{43} - \Delta H_{32} - \Delta H_{21}}{k_B T} \end{array}\right). \tag{A8}$$

At low temperature the leading term in $t(1 \rightarrow 5)$ is the exponential with the largest exponent. Therefore, the average activation energy at low temperature is:

$$\Delta H = \max\left(\begin{array}{l} \Delta H_{12}, \ \Delta H_{23}, \ \Delta H_{34}, \Delta H_{45}, \\ \Delta H_{12} + \Delta H_{23} - \Delta H_{21}, \\ \Delta H_{23} + \Delta H_{34} - \Delta H_{32}, \ \Delta H_{34} + \Delta H_{45} - \Delta H_{43}, \\ \Delta H_{12} + \Delta H_{23} + \Delta H_{34} - \Delta H_{32} - \Delta H_{21}, \\ \Delta H_{23} + \Delta H_{34} + \Delta H_{45} - \Delta H_{43} - \Delta H_{32}, \\ \Delta H_{12} + \Delta H_{23} + \Delta H_{34} + \Delta H_{45} - \Delta H_{43} - \Delta H_{32} - \Delta H_{21} \end{array}\right) \tag{A9}$$

ORCID iD

J Carter Stotts ⬥ https://orcid.org/0000-0001-7204-8693

References

[1] Girifalco L A 1964 Vacancy concentration and diffusion in order-disorder alloys *J. Phys. Chem. Solids* **25** 323–33

[2] Mishin Y and Herzig C 2000 Diffusion in the Ti–Al system *Acta Mater.* **48** 589–623

[3] Nassif R, Boughaleb Y, Hekkouri A, Gouyet J F and Kolb M 1998 Ionic diffusion on a lattice: effects of the order-disorder transition on the dynamics of non-equilibrium systems *Eur. Phys. J.* B **1** 453–64

[4] Kuper A B, Lazarus D, Manning J R and Tomizuka C T 1956 Diffusion in ordered and disordered copper-zinc *Phys. Rev.* **104** 1536–41

[5] Zhao S, Osetsky Y and Zhang Y 2019 Diffusion of point defects in ordered and disordered Ni–Fe alloys *J. Alloys Compd.* **805** 1175–83

[6] Pandey S, Koch R J, Li G, Misture S T, Wang H and Phillpot S R 2019 Thermodynamics and kinetics of ordered and disordered Cu/Au alloys from first principles calculations *J. Alloys Compd.* **809** 151615

[7] Love G R 1964 Dislocation pipe diffusion *Acta Metall.* **12** 731–7

[8] Stotts J C, Salehin R, Bakst I N, Thompson G B and Weinberger C R 2023 Hydrogen diffusion and storage in substoichiometric TiC *Int. J. Hydrog. Energy* **50** 512–23

[9] Li H, Hua W, Liu-Théato X, Fu Q, Desmau M, Missyul A, Knapp M, Ehrenberg H and Indris S 2021 New insights into lithium hopping and ordering in LiNiO$_2$ cathodes during Li (De)intercalation *Chem. Mater.* **33** 9546–59

[10] Leonidov I A, Leonidova O N, Perelyaeva L A, Samigullina R F, Kovyazina S A and Patrakeev M V 2003 Structure, ionic conduction, and phase transformations in lithium titanate Li$_4$Ti$_5$O$_{12}$ *Phys. Solid State* **45** 2183–8

[11] Balke N, Jesse S, Morozovska A N, Eliseev E, Chung D W, Kim Y, Adamczyk L, García R E, Dudney N and Kalinin S V 2010 Nanoscale mapping of ion diffusion in a lithium-ion battery cathode *Nat. Nanotechnol.* **5** 749–54

[12] Chen Y C, Ouyang C Y, Song L J and Sun Z L 2011 Lithium ion diffusion in $Li_{4+x}Ti_5O_{12}$: from Ab initio studies *Electrochim. Acta* **56** 6084–8

[13] Wagemaker M, Van Eck E R H, Kentgens A P M and Mulder F M 2009 Li-ion diffusion in the equilibrium nanomorphology of spinel $Li_{4+x}Ti_5O_{12}$ *J. Phys. Chem.* B **113** 224–30

[14] Kuganathan N, Kordatos A and Chroneos A 2019 Defect chemistry and li-ion diffusion in Li_2RuO_3 *Sci. Rep.* **9** 550

[15] Wei Yi *et al* 2015 Kinetics tuning of li-ion diffusion in layered $Li(Ni_xMn_yCo_z)O_2$ *J. Am. Chem. Soc.* **137** 26

[16] Van Der Ven A, Bhattacharya J and Belak A A 2013 Understanding li diffusion in li-intercalation compounds *Acc. Chem. Res.* **46** 1216–25

[17] Van Der Ven A, Ceder G, Asta M and Tepesch P D 2001 First-principles theory of ionic diffusion with nondilute carriers *Phys. Rev.* B **64** 184307

[18] Van Der Ven A, Aydinol M K, Ceder G, Kresse G and Hafner J 1998 First-principles investigation of phase stability in Li_xCoO_2 *Phys. Rev.* B **58** 2975–87

[19] Jang Y-I, Neudecker B J and Dudney N J 2001 Lithium diffusion in $Li_x CoO_2$ ($0.45 < x < 0.7$) intercalation cathodes *Electrochem. Solid-State Lett.* **4** A74

[20] Xia H, Lu L and Ceder G 2006 Li diffusion in $LiCoO_2$ thin films prepared by pulsed laser deposition *J. Power Sources* **159** 1422–7

[21] Gusev A I and Nazarova S Z 2005 Magnetic susceptibility of nonstoichiometric compounds of transition D-metals *Phys.-Usp.* **48** 651

[22] Lipatnikov V N, Rempel A A and Gusev A I 1997 Atomic ordering and hardness of nonstoichiometric titanium carbide *Int. J. Refract. Met. Hard Mater.* **15** 61–64

[23] Davey T and Chen Y 2022 Vacancy ordering in substoichiometric zirconium carbide: a review *Int. J. Ceram. Eng. Sci.* **4** 134–57

[24] Gusev A I and Zyryanova A N 1999 Atomic-vacancy ordering and magnetic susceptibility of nonstoichiometric hafnium carbide *J. Exp. Theor. Phys. Lett.* **69** 324–9

[25] Sarian S 1968 Anomalous diffusion of ^{14}C in $TiC_{0.67}$ *J. Appl. Phys.* **39** 5036–41

[26] Gusev A I and Rempel A A 1997 Phase diagrams of metal–carbon and metal–nitrogen systems and ordering in strongly nonstoichiometric carbides and nitrides *Phys. Status Solidi* a **163** 273–304

[27] Weinberger C R and Thompson G B 2018 Review of phase stability in the group IVB and VB transition-metal carbides *J. Am. Ceram. Soc.* **101** 4401–24

[28] Gusev A I 1991 Disorder and long-range order in non-stoichiometric interstitial compounds transition metal carbides, nitrides, and oxides *Phys. Status Solidi* b **163** 17–54

[29] Gusev A I 2000 Order–disorder transformations and phase equilibria in strongly nonstoichiometric compounds *Phys.-Usp.* **43** 1

[30] Oses C, Toher C and Curtarolo S 2020 High-entropy ceramics *Nat. Rev. Mater.* **5** 295–309

[31] Zhang R-Z and Reece M J 2019 Review of high entropy ceramics: design, synthesis, structure and properties *J. Mater. Chem.* A **7** 22148–62

[32] Akrami S, Edalati P, Fuji M and Edalati K 2021 High-entropy ceramics: review of principles, production and applications *Mater. Sci. Eng.* R **146** 100644

[33] Xiang H *et al* 2021 High-entropy ceramics: present status, challenges, and a look forward *J. Adv. Ceram.* **10** 385–441

[34] Senkov O N, Wilks G B, Miracle D B, Chuang C P and Liaw P K 2010 Refractory high-entropy alloys *Intermetallics* **18** 1758–65

[35] Li Z, Zhao S, Ritchie R O and Meyers M A 2019 Mechanical properties of high-entropy alloys with emphasis on face-centered cubic alloys *Prog. Mater. Sci.* **102** 296–345

[36] Zhang Y, Zuo T T, Tang Z, Gao M C, Dahmen K A, Liaw P K and Lu Z P 2014 Microstructures and properties of high-entropy alloys *Prog. Mater. Sci.* **61** 1–93

[37] Miracle D B and Senkov O N 2017 A critical review of high entropy alloys and related concepts *Acta Mater.* **122** 448–511

[38] Tang X, Thompson G B, Ma K and Weinberger C R 2022 The role of entropy and enthalpy in high entropy carbides *Comput. Mater. Sci.* **210** 111474

[39] Miracle D B 2019 High entropy alloys as a bold step forward in alloy development *Nat. Commun.* **10** 1805

[40] George E P, Curtin W A and Tasan C C 2020 High entropy alloys: a focused review of mechanical properties and deformation mechanisms *Acta Mater.* **188** 435–74

[41] George E P, Raabe D and Ritchie R O 2019 High-entropy alloys *Nat. Rev. Mater.* **4** 515–34

[42] Li W, Xie D, Li D, Zhang Y, Gao Y and Liaw P K 2021 Mechanical behavior of high-entropy alloys *Prog. Mater. Sci.* **118** 100777

[43] Beke D L and Erdélyi G 2016 On the diffusion in high-entropy alloys *Mater. Lett.* **164** 111–3

[44] Dąbrowa J, Zajusz M, Kucza W, Cieślak G, Berent K, Czeppe T, Kulik T and Danielewski M 2019 Demystifying the sluggish diffusion effect in high entropy alloys *J. Alloys Compd.* **783** 193–207

[45] Yeh J-W, Chen S-K, Lin S-J, Gan J-Y, Chin T-S, Shun T-T, Tsau C-H and Chang S-Y 2004 Nanostructured high-entropy alloys with multiple principal elements: novel alloy design concepts and outcomes *Adv. Eng. Mater.* **6** 299–303

[46] Vattulainen I, Ying S C, Ala-Nissila T and Merikoski J 1999 Memory effects and coverage dependence of surface diffusion in a model adsorption system *Phys. Rev.* B **59** 7697–707

[47] Ying S C, Vattulainen I, Merikoski J, Hjelt T and Ala-Nissila T 1998 Memory expansion for diffusion coefficients *Phys. Rev.* B **58** 2170–8

[48] Gosálvez M A and Alberdi-Rodriguez J 2017 Microscopic origin of the apparent activation energy in diffusion-mediated monolayer growth of two-dimensional materials *J. Phys. Chem.* C **121** 20315–22

[49] Alberdi-Rodriguez J, Acharya S R, Rahman T S, Arnau A and Gosálvez M A 2020 Dominant contributions to the apparent activation energy in two-dimensional submonolayer growth: comparison between Cu/Ni(111) and Ni/Cu(111) *J. Phys.: Condens. Matter* **32** 445002

[50] Gosalvez M A and Alberdi-Rodriguez J 2018 A microscopic perspective on heterogeneous catalysis (arXiv:1812.11398v1)

[51] Cipra B A 1987 An introduction to the Ising model *Am. Math. Mon.* **94** 937–59

[52] Grandi B C S and Figueiredo W 1999 Monte Carlo simulation of an antiferromagnetic Ising model at two competing temperatures *Phys. Rev.* E **59** 4992–6

[53] Grandi B C S and Figueiredo W 1997 Monte Carlo simulation of an Ising antiferromagnet with competing Glauber and Kawasaki dynamics *Phys. Rev.* E **56** 5240–4

[54] Kalz A, Honecker A, Fuchs S and Pruschke T 2009 Monte Carlo studies of the Ising square lattice with competing interactions *J. Phys.: Conf. Ser.* **145** 012051

[55] Jin S, Sen A, Guo W and Sandvik A W 2013 Phase transitions in the frustrated Ising model on the square lattice *Phys. Rev.* B **87** 144406

[56] Kawasaki K 1966 Diffusion constants near the critical point for time-dependent Ising models. I *Phys. Rev.* **145** 224–30

[57] Evans M G and Polanyi M 1938 Inertia and driving force of chemical reactions *Trans. Faraday Soc.* **34** 11–24

[58] Cowley J M 1965 Short-range order and long-range order parameters *Phys. Rev.* **138** A1384–A1389

[59] Cowley J M 1950 An approximate theory of order in alloys *Phys. Rev.* **77** 669–75

[60] Swalin R A 1972 *Thermodynamics of Solids* (Wiley)

[61] Onsager L 1944 Crystal statistics. I. A two-dimensional model with an order-disorder transition *Phys. Rev.* **65** 117–49

[62] Di Stefano D, Nazarov R, Hickel T, Neugebauer J, Mrovec M and Elsässer C 2016 First-principles investigation of hydrogen interaction with TiC precipitates in α -Fe *Phys. Rev. B* **93** 184108